nature nanotechnology

ARTICLES

PUBLISHED ONLINE: 19 JUNE 2017 | DOI: 10.1038/NNANO.2017.111

Monitoring the orientation of rare-earth-doped nanorods for flow shear tomography

Jongwook Kim[1]*, Sébastien Michelin[2], Michiel Hilbers[3], Lucio Martinelli[1], Elodie Chaudan[1], Gabriel Amselem[2], Etienne Fradet[2], Jean-Pierre Boilot[1], Albert M. Brouwer[3], Charles N. Baroud[2], Jacques Peretti[1] and Thierry Gacoin[1]*

Rare-earth phosphors exhibit unique luminescence polarization features originating from the anisotropic symmetry of the emitter ion's chemical environment. However, to take advantage of this peculiar property, it is necessary to control and measure the ensemble orientation of the host particles with a high degree of precision. Here, we show a methodology to obtain the photoluminescence polarization of Eu-doped $LaPO_4$ nanorods assembled in an electrically modulated liquid-crystalline phase. We measure Eu^{3+} emission spectra for the three main optical configurations (σ, π and α, depending on the direction of observation and the polarization axes) and use them as a reference for the nanorod orientation analysis. Based on the fact that flowing nanorods tend to orient along the shear strain profile, we use this orientation analysis to measure the local shear rate in a flowing liquid. The potential of this approach is then demonstrated through tomographic imaging of the shear rate distribution in a microfluidic system.

Luminescent particles or molecules are widely used for labelling and tracking of small objects. Anisotropic emitters such as semiconductor nanowires[1], quantum rods[2] or organic dyes[3] exhibit polarized luminescence, providing an additional sensitivity to the orientation[4]. The polarization is, in most cases, dominated by the size and shape anisotropy of the emitter particle[1,2], which is understood within the quantum size effect and the electric field confinement effect on both the excitation and emission processes[5–8]. The photoluminescence of rare-earth phosphors, however, shows a distinguished nature of emission polarization. The photoluminescence spectrum of lanthanide ions in a crystalline host matrix consists of many sharp peaks due to the multiple transition levels within the 4*f* configuration and their crystal-field splitting into degenerate sublevels[9,10]. Each sublevel emission is polarized along a particular direction allowed by the crystallographic symmetry. Consequently, the emission spectrum from a single crystal manifests variation of its line shape when the crystal's orientation changes with respect to the direction of polarization analysis[11–14]. This phenomenon is independent of the particle size and morphology, and is decoupled from the polarization of the usually indirect excitation, which is a crucial advantage for the orientation analysis when compared to the other types of anisotropic emitter.

A prerequisite for precise orientation analysis is to acquire the reference photoluminescence polarization components, which requires either working with a single crystal or achieving a uniform orientation of small crystallites. Here, we use liquid-crystalline (LC) self-assembly of monocrystalline $LaPO_4$:Eu nanorods[15,16] that exhibit polarized photoluminescence, as from a large single crystal. By electrically switching the orientation of the LC domain[17], in a manner similar to the approach by Galyametdinov *et al.* with organic lanthanidomesogens[18], polarized Eu^{3+} emission spectra could be selectively obtained for the three main configurations (σ and π, the radial propagations polarized perpendicular and parallel to the rod axis, respectively, and α, the isotropic axial propagation). We show that the distinct σ–π–α line shapes allow us to determine the unknown three-dimensional rod orientation and also the collective degree of orientation of an ensemble of nanorods, thereby establishing a route to the *in situ* study of rod-orientation dynamics.

We apply this method to measure the local shear rate in a flowing liquid that imposes the orientation of colloidally dispersed nanorods. The orientation of anisotropic objects under flow is a ubiquitous effect. The local orientation director **n** and the order parameter *f* are directly correlated with the principal direction and intensity of the shear rate[19,20]. Accordingly, scanning **n** and *f* should allow one to retrieve the time-dependent shear rate distribution, which is of particular interest when studying microfluidic and biofluidic systems[21–24]. The currently available particle imaging velocimetry (PIV) technique, which measures the flow velocity profile by tracking the displacements of fluorescent microspheres[25,26], requires heavy accumulation and post-treatment of image frames. This limits access to the local real-time observation of dynamic systems. Moreover, the signal-to-noise ratio and the spatial resolution of PIV deteriorate when the principal interest is in shear (gradient of velocity). Our approach aims to achieve direct measurement and fast scanning of the local shear rate by instantly detecting the collective orientation of nanorods in a small focal volume. As a proof of concept, we demonstrate tomographic mapping of the shear distribution in a microfluidic channel using scanning confocal microscopy.

Polarized photoluminescence from assembled nanorods

Figure 1a presents polarized photoluminescence spectra from a nematic LC suspension of $LaPO_4$:Eu nanorods modulated in an electro-optical cell. The most intense $^5D_0$–$^7F_1$ (magnetic dipole) transition and the adjacent $^5D_0$–$^7F_2$ (electric dipole) transition spectra, both consisting of multiple sublevel peaks, were collected under excitation of the $^7F_0$–$^5L_6$ transition at 394 nm (the excitation spectrum is shown in Supplementary Fig. 3). An optical transmission microscopy image of the cell placed between crossed

[1]Laboratoire de Physique de la Matière Condensée, Ecole Polytechnique, CNRS, Université Paris-Saclay, 91128 Palaiseau, France. [2]Laboratoire d'Hydrodynamique (LadHyX), Ecole Polytechnique, CNRS, Université Paris-Saclay, 91128 Palaiseau, France. [3]van 't Hoff Institute for Molecular Sciences, University of Amsterdam, PO Box 94157, 1090 GD Amsterdam, The Netherlands. *e-mail: jong-wook.kim@polytechnique.edu; thierry.gacoin@polytechnique.edu

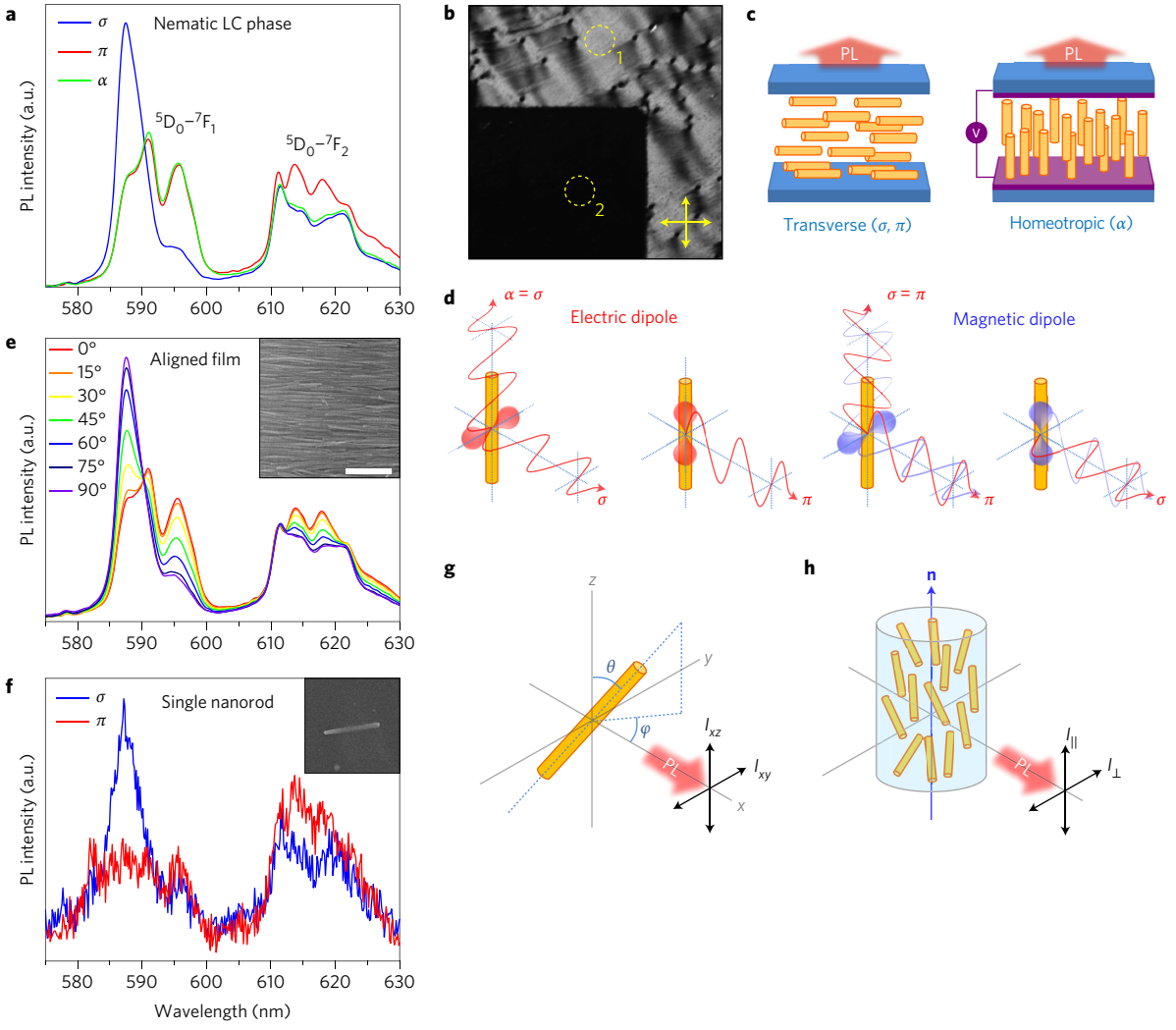

Figure 1 | Polarized photoluminescence of $LaPO_4$:Eu nanorods. a, Photoluminescence (PL) spectra in the σ, π and α configurations obtained from the nematic LC suspension of $LaPO_4$:Eu nanorods with transverse and homeotropic orientations. **b**, Optical transmission microscopy image of the electro-optical switching cell filled with the nematic suspension. The image dimensions are 1.8 mm × 1.8 mm. The cell was placed between crossed polarizers (indicated by arrows). The inverted L-shaped bright region is where the nematic domain was transversely oriented due to the capillary invasion. The wavy texture was generated due to the 20-μm-thick silica bead spacers (black dots dispersed in the bright region). The dark rectangular region corresponds to the area (delimited by the top and bottom transparent electrodes of the cell) where a longitudinal electric field was applied to obtain homeotropic orientation. Dotted circles '1' and '2' indicate the transverse and homeotropic zones where the polarized photoluminescence spectra shown in **a** were collected. **c**, Schematic illustration of the transverse and homeotropic orientations of the nanorods in the cell. **d**, Schematic illustration of the contributions of electric dipole transition and magnetic dipole transition in the σ, π and α configurations. **e**, Polarized photoluminescence spectra obtained from an aligned thin film of $LaPO_4$:Eu nanorods fabricated by the shear-directed assembly. Analyser angle θ was changed in 15° steps. Inset: scanning electron microscopy (SEM) image of the film (scale bar, 200 nm). **f**, Polarized photoluminescence spectra (σ and π configurations) obtained from a single nanorod using a confocal microscope. The position and orientation of the nanorod were detected using SEM and atomic force microscopy (AFM; Supplementary Fig. 2). Inset: SEM image of the same nanorod (rod length of ~500 nm). **g**, Schematic illustration of a nanorod with an angular orientation (θ, φ) with respect to the photoluminescence measurement plane (y–z plane). **h**, Schematic illustration of a preferential partial orientation of colloidal nanorods due to an external stimulus and of transverse photoluminescence measurements $I_{||}$ and $I_{\perp}$.

polarizers (Fig. 1b) shows a bright region exhibiting in-plane birefringence induced by the transverse rod alignment, as schematized in Fig. 1c, left. A uniform LC domain orientation was directed by shear strain applied during the capillary invasion of the viscous suspension into the 20-μm-thick gap of the cell (for the cell geometry see Supplementary Fig. 1). The blue and red curves in Fig. 1a were obtained from this transverse region (dotted circle labelled '1' in Fig. 1b) with an analyser perpendicular and parallel to the domain orientation, respectively. Considering the hexagonal symmetry of $LaPO_4$:Eu, with the crystallographic c axis parallel to the long axis of the rod[27], these two spectra correspond to the mutually orthogonal polarization components referred to as σ and π configurations (Fig. 1d). The difference in their line shapes is due to the independent polarization of each sublevel emission originating from the crystal-field splitting[9]. When the electric field was applied longitudinally in the cell gap (Fig. 1c, right), the nematic domain, initially in a transverse state, was switched to a homeotropic state where the birefringence vanished completely (dark square region in Fig. 1b) as a consequence of the rod alignment being along the field normal to the substrate plane. The α spectrum (green line in Fig. 1a) corresponding to the axial propagation (Fig. 1d) was obtained from this homeotropic region (dotted circle '2' in Fig. 1b). In contrast to the σ and π spectra, the α spectrum was unchanged when rotating the analyser, because the

axial symmetry of the crystal produces isotropic polarization contributions in the c plane.

The σ and π spectra were also confirmed with two different types of sample, where the rod orientation was directly observable by scanning electron microscopy (SEM). First, a thin film with transverse rod alignment (Fig. 1e, inset) was prepared by directed assembly of a nematic gel suspension[28]. The polarized photoluminescence spectra observed from this solid film (Fig. 1e) with analyser angle θ perpendicular ($\theta = 90°$) and parallel ($\theta = 0°$) to the rod orientation are identical to the σ and π spectra obtained from the LC sample (Fig. 1a). Moreover, the tendency of the line shape variation with θ supports that the polarization of the Eu^{3+} emission is subject to the uniaxial symmetry of the crystalline $LaPO_4$ matrix. A peak deconvolution study of the $^5D_0$–$^7F_1$ transition shows that the sublevel peak intensity I_θ as a function of θ closely fits the trigonometric equation $I_\theta = I_\sigma \sin^2\theta + I_\pi \cos^2\theta$, where I_σ and I_π indicate the peak intensities in the σ and π spectra (Supplementary Figs 4–5). Furthermore, the polarized emission spectra taken from a single nanorod (Fig. 1f) show the same σ and π spectral line shapes, verifying that the observed polarization behaviour originates exclusively from the intrinsic crystal structure and not from the collective effect of the assembled structure.

Three-dimensional orientation analysis

Note that the α spectrum is identical to the π spectrum in the $^5D_0$–$^7F_1$ (magnetic dipole) band and the σ spectrum in the $^5D_0$–$^7F_2$ (electric dipole) band (Fig. 1a). This can be understood considering that the radiation electric field is parallel to the electric dipole and perpendicular to the magnetic dipole (Fig. 1d). This peculiar aspect of polarization offers the opportunity to measure the three-dimensional rod orientation precisely. Defining the rod orientation in the laboratory frame by the polar and azimuthal angles (θ, φ) (Fig. 1g), it is possible to express the two measured polarized photoluminescence intensities I_{xy} and I_{xz} (the two indices refer to the axis of propagation and the axis parallel to the analyser, respectively) as functions of θ and φ. In the case of the magnetic dipole transition,

$$I_{xy} = I_\sigma \cos^2\theta + I_\pi \sin^2\theta \quad (1)$$

$$I_{xz} = I_\sigma \sin^2\theta \ \sin^2\varphi + I_\pi(\cos^2\theta \ \sin^2\varphi + \cos^2\varphi) \quad (2)$$

where I_σ and I_π indicate the relative intensities of the σ and π configurations. By solving these equations simultaneously with their equivalents for the electric dipole transition (Supplementary equations (4) and (5)), one can determine the set of (θ, φ) without consideration of the absolute intensities. Errors that may occur with the overall signal fluctuation from any extrinsic parameter can be avoided in this ratiometric line shape analysis. When regarding an ensemble of nanorods that acquires a partial orientation toward a preferential direction (Fig. 1h), the order parameter, defined by $f = (3\cos^2\theta - 1)/2$, can be deduced from the following equations (written here also for the magnetic dipole transition):

$$I_\perp = I_\sigma \langle\cos^2\theta\rangle + I_\pi(1 - \langle\cos^2\theta\rangle) \quad (3)$$

$$2I_{||} = I_\sigma(1 - \langle\cos^2\theta\rangle) + I_\pi(1 + \langle\cos^2\theta\rangle) \quad (4)$$

where $I_\perp$ and $I_{||}$ indicate the two polarized photoluminescence intensities perpendicular and parallel to **n**. A complete description for obtaining **n** (similar to the way of obtaining θ and φ for a single nanorod) and then $I_\perp$ and $I_{||}$ from a system with unknown **n** is provided in Supplementary Section II.

Flow shear measurement

This capability to analyse the collective rod orientation was used to probe the local arrangement of nanorods induced by the shear flow. The stress-optical law describes the direct correlation between the shear rate ($\dot\gamma$) and f, which is proportional to the induced flow birefringence (Δn)[29–31]. Measuring Δn allows us to deduce the value of $\dot\gamma$ and the related rheological parameters of fluids[32]. The rheological properties of bulk fluids have often been studied in this way[33]. However, so far, the stress-optical method has not been applicable to local measurements because birefringence is an integrated signal throughout the whole light pathway across the medium. Polarized photoluminescence, in contrast, enables a microscopic focal volume in the middle of the medium to be addressed. Local stress-optical analysis and three-dimensional mapping can therefore be attempted when taking advantage of the high sensitivity and resolution provided by confocal microscopy.

We first studied the flow of a dilute colloidal nanorod suspension in a capillary tube. Figure 2a schematically shows the general aspect of the rod orientation in a Poiseuille flow. Rods are highly oriented near the wall where a large shear stress ($\tau = \mu \cdot \dot\gamma$, where μ is dynamic viscosity) is applied, and are disordered at the centre where τ approaches to zero. The photoluminescence spectrum observed from the whole capillary volume should be partially polarized in correlation with the average shear rate ($\dot\gamma$), which is proportional to the flow rate. Figure 2b shows the intensity variation of a polarized photoluminescence emission peak $I_\perp$ ($\lambda = 587$ nm, observed with an analyser perpendicular to the capillary) while increasing the flow rate in steps. The initially disordered nanorods start to orient when the suspension flows. The increment of $I_\perp$ is directly proportional to f, according to equation (3). Even a very small change in the flow rate of 5 µl min^{-1} (~0.1 mm s^{-1} in average velocity) produces an appreciable change in $I_\perp$, ensuring the high sensitivity of the method.

To examine the validity of this polarized photoluminescence-based stress-optical measurement, it is necessary to compare it with the traditional method based on birefringence measurement. An experiment was implemented using a microfluidic channel with a rectangular cross-section, from which the photoluminescence and birefringence could be simultaneously observed. Figure 2c displays the gradual increase of flow birefringence when increasing the flow rate, which can be converted into $\dot\gamma$. The corresponding polarized photoluminescence line shape, collected from a section of the channel volume with an analyser perpendicular to the flow direction, also changes towards the shape of the σ spectrum, implying higher f with higher $\dot\gamma$ (Fig. 2d). The optical retardation ($\delta = \Delta n \cdot d$, where d is the channel thickness) profiles across the channel width for different $\dot\gamma$ are shown in Fig. 2e. These profiles represent the integrated birefringence through the channel depth. The δ value at the channel centre is non-zero due to the contribution of shear at the top and bottom surfaces of the channel. This illustrates why local stress-optical analysis cannot be achieved by birefringence measurements alone. In Fig. 2f, the δ values averaged over the image plane are plotted (green circles) along with the f values deduced from the line shape analysis of the polarized photoluminescence spectra (red triangles) collected over the same image plane. These two independently measured quantities display an identical evolution as a function of $\dot\gamma$ (bottom abscissa axis). An excellent agreement is also found with a theoretical calibration curve for f (blue line) as a function of $\dot\gamma/\Omega$ (top abscissa axis)[34] when Ω, the rotational diffusion coefficient, was set to be 0.5 s^{-1} for the best fitting. Theoretically, Ω is given as

$$\Omega = \frac{3k_B T}{16\pi\eta_0 a^3}\left(-1 + 2\ln\frac{2a}{b}\right) \quad (5)$$

where k_B is the Boltzmann constant, η_0 is the solvent viscosity, and a and b, respectively, are the half-length and equatorial radius of the

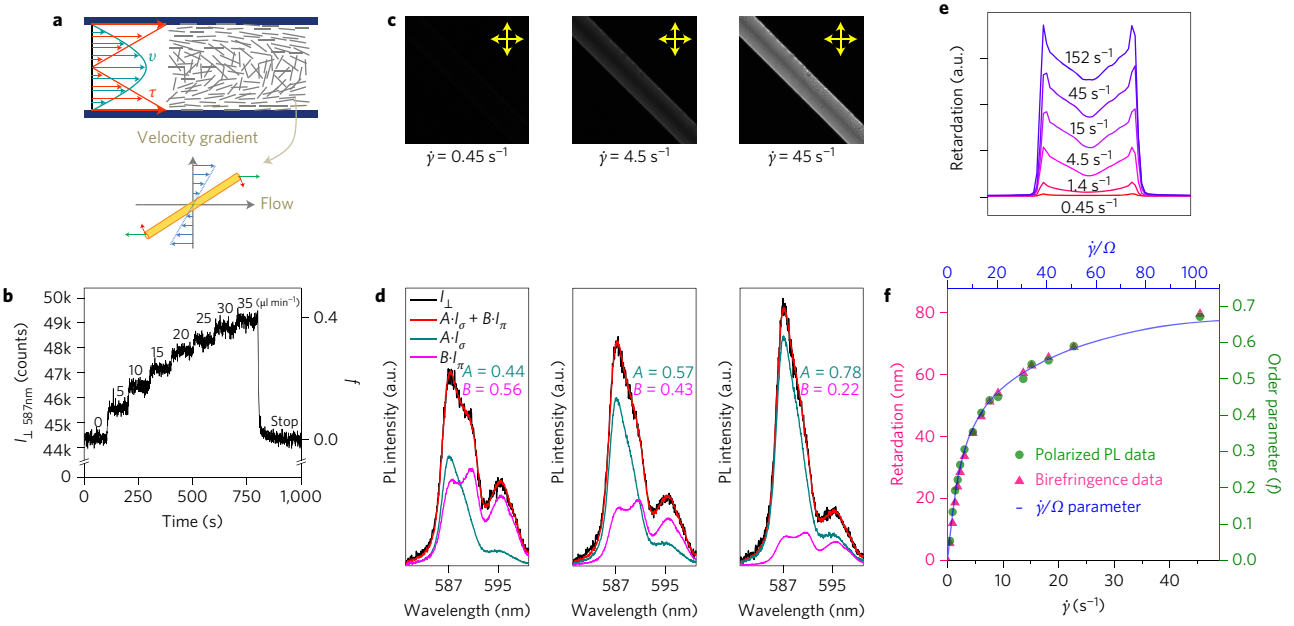

Figure 2 | Stress-optical measurements of a flowing nanorod suspension. a, Schematic illustration of the orientation of colloidal nanorods under Poiseuille flow with typical velocity (v) and shear stress (τ) profiles. **b**, Flow rate-dependent photoluminescence (PL) intensity at λ = 587 nm from a colloidal $LaPO_4$:Eu nanorod suspension (0.9 vol% in ethylene glycol) flowing in a capillary tube (diameter = 1 mm). Flow rate was increased in steps of 5 µl min^{-1} each 100 s. **c**, Optical transmission microscopy image of the same suspension flowing through a rectangular microfluidic channel (100 µm width, 50 µm height) for three different average shear rates ($\dot{\gamma}$). The channel was placed between crossed polarizers (indicated by arrows). **d**, Polarized photoluminescence spectra of the $^5D_0$–$^7F_1$ transition (black line) and the fit (red line) by the weighted sum of I_σ (cyan line) and I_π (pink line). Values of $A = \cos^2\theta$ and $B = 1 - \cos^2\theta$, the weight coefficients of I_σ and I_π obtained from the fit, are indicated. **e**, Optical retardation (δ) profiles across the channel width at different $\dot{\gamma}$. **f**, Variations of average δ (pink triangles) and average order parameter obtained by analysis of the polarized photoluminescence spectra (green circles) as functions of $\dot{\gamma}$. The blue line is a theoretical calibration curve as a function of $\dot{\gamma}/\Omega$ fit with the stress-optical law.

particle[20]. The Ω value calculated with the measured viscosity and average nanorod size is 10 s^{-1}, which is an order of magnitude greater than 0.5 s^{-1} from the calibration curve fitting. We estimate that the collective behaviour of nanorods with surface charge-mediated long-range repulsive interactions or size polydispersity are responsible for such a difference.

The above results guarantee a reliable stress-optical measurement by analysing the polarized photoluminescence of colloidal $LaPO_4$:Eu nanorods. On this basis, local detection of $\dot{\gamma}$ was tested for a geometrically complex flow generated in a microfluidic channel with a constriction (Fig. 3a). Confocal microscopy with laser excitation at 394 nm ($^7F_0$–$^5L_6$ transition) was performed for the local photoluminescence measurement. The polarized photoluminescence spectra emitted from focal spots positioned at the channel wall and centre (indicated by red arrows in Fig. 3a) are plotted in Fig. 3b. At the wall, where $\dot{\gamma}$ reaches its maximum, the two spectra obtained with analyser angles of 0° and 90° exhibit contrasting line shapes that are close to the π and σ spectra, respectively. However, at the channel centre, the two spectra are almost identical, because $\dot{\gamma}$ approaches zero. When the flow rate was abruptly changed, the resulting spectral fluctuation at a fixed focal position could be recorded with the time resolution available with the spectrometer.

The scanning operation of the confocal microscope allowed the construction of tomographic maps of such a local shear measurement over any scanning section. Figure 3c presents polarized photoluminescence intensity maps for a peak wavelength of 587 nm over vertical and horizontal scanning sections (Fig. 3a). From each set of these intensity maps, a corresponding map of the apparent shear rate ($\dot{\gamma}_{app}$) can be constructed by simple image processing using equations (3) and (4) and the f versus $\dot{\gamma}$ calibration curve in Fig. 3f. Note that, because the f versus $\dot{\gamma}$ curve is not linear, the accuracy of the determination of $\dot{\gamma}_{app}$ should depend on its value. However, the relative uncertainty, $\Delta\dot{\gamma}/\dot{\gamma}$, estimated from the derivative of the f versus $\dot{\gamma}$ curve, varies weakly as soon as $\dot{\gamma}/\Omega > 1$ (Supplementary Fig. 6). This is advantageous for an accurate determination of $\dot{\gamma}_{app}$ in a wide range extending over 100 s^{-1}. The $\Delta\dot{\gamma}/\dot{\gamma}$ value in our experiment is smaller than 30%. Figure 3d shows a surface plot of the $\dot{\gamma}_{app}$ profile over the vertical scanning section. In this case, the local director of $\dot{\gamma}$, that is, the principal shear direction, is constantly normal to the scanning plane. This $\dot{\gamma}_{app}$ profile is similar to the inverted pyramidal shape theoretically predicted for a Poiseuille flow in a rectangular channel. This result implies the near-Newtonian rheology of the dilute $LaPO_4$:Eu nanorod suspension, which thus seems to be suited for performing the stress-optical analysis. Meanwhile, the $\dot{\gamma}_{app}$ map constructed over the horizontal scanning section with the semicircular constriction (Fig. 3e, the colour represents the quantity of $\dot{\gamma}_{app}$ and the arrows indicate **n**) shows an unexpected asymmetric profile. Considering the small channel dimension and flow rate (Reynolds number of ~10^{-3}), inertia plays a negligible role here and the flow regime is purely viscous, which should lead to a fore-aft symmetry for Newtonian fluids[35], as can be seen from a theoretically modelled $\dot{\gamma}$ map (Supplementary Fig. 8a). However, in Fig. 3e, the region of maximum $\dot{\gamma}_{app}$ (that is, maximum f) is deviated towards the upstream (left side) and away from the constriction wall. Similar asymmetric birefringence profiles have also been reported in the study of viscoelastic polymer suspensions[36].

Computational analysis

Examining the asymmetry of the $\dot{\gamma}_{app}$ map (Fig. 3e) is imperative for establishing a reliable stress-optical analysis. Therefore, we conducted a computational analysis of the rod-orientation dynamics. The details of the method and results are provided in Supplementary Section III and Supplementary Fig. 7. This study reveals that the discrepancy between $\dot{\gamma}_{app}$ and the real shear rate $\dot{\gamma}$ originates in the advection and non-instantaneous reorientation of

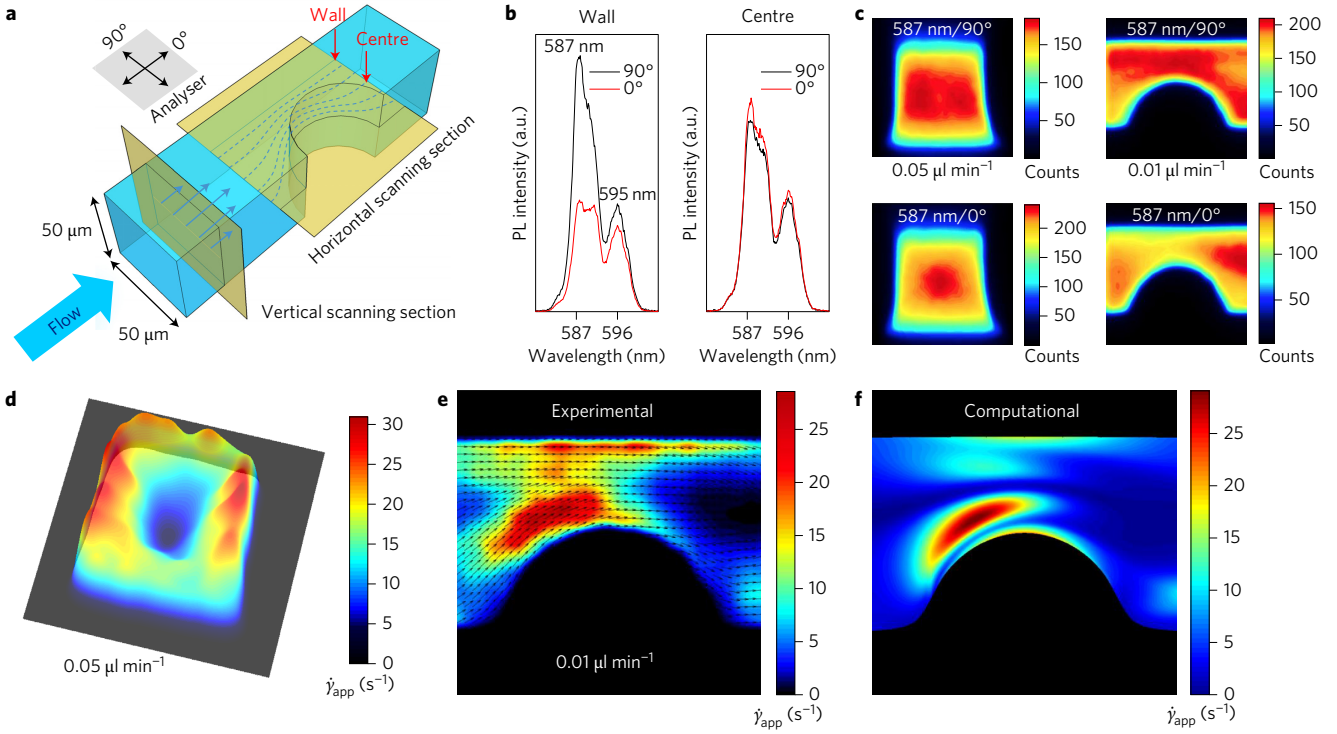

Figure 3 | Tomographic stress-optical analysis of a microfluidic system. a, Schematic illustration of the microfluidic channel used for the local shear rate measurement. The channel has a square-shaped cross-section (50 × 50 μm) and a semicircular constriction (diameter = 50 μm). Two photoluminescence (PL) scanning sections are shown as yellow planes. The horizontal section is placed at the middle height of the channel and includes the constriction. Analyser angles θ of 0° and 90° correspond to the directions parallel and perpendicular to the channel length on the observation plane parallel to the horizontal scanning section. **b**, Polarized photoluminescence spectra (θ = 0° and 90°) of the $^5D_0$–$^7F_1$ transition collected at the channel wall and centre positions as indicated with red arrows in **a**. **c**, Colour maps of the polarized photoluminescence intensity (θ = 0° and 90°) centred at λ = 587 nm selected by a bandpass filter. The left two images were obtained on the vertical scanning section with a flow rate of 0.05 μl min^{-1}. The right two images were obtained on the horizontal scanning section with a flow rate of 0.01 μl min^{-1}. The colour bars are scaled in number of counts per pixel. **d**, Three-dimensional colour map of the apparent shear rate on the vertical scanning section. **e**, Colour map of $\dot{\gamma}_{app}$ superposed with a vector map of **n** on the horizontal scanning section. The maps in **d** and **e** were obtained by stress-optical analysis of the polarized photoluminescence intensity maps shown in **c**. **f**, Computationally obtained $\dot{\gamma}_{app}$ map with the Peclet number set to 5.

the nanorods in a non-homogeneous flow. When the streamlines are not parallel around the constriction, the nanorods advected by the flow experience time-dependent local shear that varies over a typical timescale $\tau_a = H/U$ (where H is the channel width and U the flow velocity) taken to flow over the constriction. However, the response of the probability distribution for the nanorods' orientation occurs on the rotational diffusion timescale $\tau_d = \Omega^{-1}$. The Peclet number is the ratio of these two timescales, $Pe = U/H\Omega$, and measures the relative rates of advection and diffusion. For small Pe, the response is instantaneous, and the stress-optical law holds everywhere, whereas for intermediate to large Pe, the orientation of individual particles depends on the local shear but also on the shear to which the particles have been exposed previously, leading to history effects. Indeed, the computationally obtained $\dot{\gamma}_{app}$ map for Pe = 0.5 (Supplementary Fig. 8b) is almost identical to the theoretical $\dot{\gamma}$ map, which is symmetric (Supplementary Fig. 8a). However, the Pe given for our experiment is 5 when applying the $\Omega = 0.5$ s^{-1} obtained from the calibration curve (Fig. 2f). History effects are thus non-negligible and explain the discrepancy between the apparent and real shear rates: the computationally obtained $\dot{\gamma}_{app}$ map for Pe = 5 (Fig. 3f) matches well the experimental $\dot{\gamma}_{app}$ map (Fig. 3e), both qualitatively (highly ordered upstream and rapid loss of orientation coherence downstream) and quantitatively.

These computational results suggest that, to produce reliable $\dot{\gamma}_{app}$ maps, the Pe number need to be small enough to suppress the history effects. This can be realized by reducing the particle size, which would rapidly increase Ω (equation (5)). We estimate that if the $LaPO_4$:Eu nanorod size is reduced by a factor of three (Pe = 0.2), the stress-optical analysis and the tomographic $\dot{\gamma}$ mapping would be satisfactory for most microfluidic systems of interest.

Conclusions

We have presented a simple method to measure the polarized photoluminescence spectra (in σ, π and α configurations) of $LaPO_4$:Eu nanorods from their electrically modulated liquid-crystalline phase. The three-dimensional orientation of an individual nanorod or the director (**n**) and order parameter (f) of a rod assembly can be precisely determined by analysing their polarized photoluminescence line shape. This approach allowed us to investigate the rod-orientation dynamics of the colloidal nanorods flowing in a microfluidic channel. The local shear rate ($\dot{\gamma}$) profiles over sections of the fluid volume were deduced based on the stress-optical law. A reliable estimation of the $\dot{\gamma}$ profile was obtained over a region where the stream lines are parallel. However, a discrepancy between theory and experiment was found for non-parallel flows involving rod advection and reorientation. A computational study verified that this discrepancy is due to the non-instantaneous reorientation of nanorods and that it could be effectively suppressed by decreasing the nanorod size. With further optimization of the nanorod size, this technique is promising in that it yields a straightforward stress-optical method for tomographic mapping and real-time monitoring of local $\dot{\gamma}$ with the high spatial resolution necessary for applications in microfluidics and biofluidics. Furthermore, the

presented orientation analysis might be exploited for the study of the complex dynamics of other microscopic systems (such as cells, genes and enzymes) by using rare-earth luminophores as orientation markers.

Methods

Methods and any associated references are available in the online version of the paper.

Received 4 August 2015; accepted 5 May 2017;
published online 19 June 2017

References

1. Wang, J., Gudiksen, M. S., Duan, X., Cui, Y. & Lieber, C. M. Highly polarized photoluminescence and photodetection from single indium phosphide nanowires. *Science* **293,** 1455–1457 (2001).
2. Hu, J. *et al.* Linearly polarized emission from colloidal semiconductor quantum rods. *Science* **292,** 2060–2063 (2001).
3. Forkey, J. N., Quinlan, M. E., Shaw, M. A., Corrie, J. E. T. & Goldman, Y. E. Three-dimensional structural dynamics of myosin V by single-molecule fluorescence polarization. *Nature* **422,** 399–404 (2003).
4. Ohmachi, M. *et al.* Fluorescence microscopy for simultaneous observation of 3D orientation and movement and its application to quantum rod-tagged myosin V. *Proc. Natl Acad. Sci. USA* **109,** 5294–5298 (2012).
5. Wang, Y. & Herron, N. Nanometer-sized semiconductor clusters: materials synthesis, quantum size effects, and photophysical properties. *J. Phys. Chem.* **95,** 525–532 (1991).
6. McIntyre, C. R. & Sham, L. J. Theory of luminescence polarization anisotropy in quantum wires. *Phys. Rev. B* **45,** 9443–9446 (1992).
7. Califano, M. & Zunger, A. Anisotropy of interband transitions in InAs quantum wires: an atomistic theory. *Phys. Rev. B* **70,** 165317 (2004).
8. Chen, H.-Y., Yang, Y.-C., Lin, H.-W., Chang, S.-C. & Gwo, S. Polarized photoluminescence from single GaN nanorods: effects of optical confinement. *Opt. Express* **16,** 13465–13475 (2008).
9. Binnemans, K. & Görller-Walrand, C. C. A. Application of the Eu^{3+} ion for site symmetry determination. *J. Rare Earth.* **14,** 173–180 (1996).
10. Hänninen, P. H., Ala-Kleme, T. & Hèarmèa, H. *Lanthanide Luminescence: Photophysical, Analytical and Biological Aspects* (Springer, 2011).
11. Sayre, E. V. & Freed, S. Spectra and quantum states of the europic ion in crystals. II. Fluorescence and absorption spectra of single crystals of europic ethylsulfate nonahydrate. *J. Chem. Phys.* **24,** 1213–1219 (1956).
12. Brecher, C., Samelson, H., Lempicki, A., Riley, R. & Peters, T. Polarized spectra and crystal-field parameters of Eu^{+3} in YVO_4. *Phys. Rev.* **155,** 178–187 (1967).
13. DeShazer, L. G. & Dieke, G. H. Spectra and energy levels of Eu^{3+} in $LaCl_3$. *J. Chem. Phys.* **38,** 2190–2199 (1963).
14. Brecher, C. Europium in the ultraphosphate lattice: polarized spectra and structure of EuP_5O_{14}. *J. Chem. Phys.* **61,** 2297–2315 (1974).
15. Kim, J. *et al.* $LaPO_4$ mineral liquid crystalline suspensions with outstanding colloidal stability for electro-optical applications. *Adv. Funct. Mater.* **22,** 4949–4956 (2012).
16. Onsager, L. The effects of shape on the interaction of colloidal particles. *Ann. NY Acad. Sci.* **51,** 627–659 (1949).
17. Kim, J. *et al.* Optimized combination of intrinsic and form birefringence in oriented $LaPO_4$ nanorod assemblies. *Appl. Phys. Lett.* **105,** 061102 (2014).
18. Galyametdinov, Y. G. *et al.* Polarized luminescence from aligned samples of nematogenic lanthanide complexes. *Adv. Mater.* **20,** 252–257 (2008).
19. Bretherton, F. P. The motion of rigid particles in a shear flow at low Reynolds number. *J. Fluid Mech.* **14,** 284–304 (1962).
20. Cerf, R. & Scheraga, H. A. Flow birefringence in solutions of macromolecules. *Chem. Rev.* **51,** 185–261 (1952).
21. Fisher, A. B., Chien, S., Barakat, A. I. & Nerem, R. M. Endothelial cellular response to altered shear stress. *Am. J. Physiol. Lung Cell. Mol. Physiol.* **281,** L529–L533 (2001).
22. Baroud, C. N., Gallaire, F. & Dangla, R. Dynamics of microfluidic droplets. *Lab Chip* **10,** 2032–2045 (2010).
23. Oddy, M. H., Santiago, J. G. & Mikkelsen, J. C. Electrokinetic instability micromixing. *Anal. Chem.* **73,** 5822–5832 (2001).
24. El-Ali, J., Sorger, P. K. & Jensen, K. F. Cells on chips. *Nature* **442,** 403–411 (2006).
25. Lindken, R., Rossi, M., Große, S. & Westerweel, J. Micro-particle image velocimetry (μPIV): recent developments, applications, and guidelines. *Lab Chip* **9,** 2551–2567 (2009).
26. Lee, S. J. & Kim, S. Advanced particle-based velocimetry techniques for microscale flows. *Microfluid. Nanofluid.* **6,** 577–588 (2009).
27. Fang, Y.-P. *et al.* Systematic synthesis and characterization of single-crystal lanthanide orthophosphate nanowires. *J. Am. Chem. Soc.* **125,** 16025–16034 (2003).
28. Kim, J., Peretti, J., Lahlil, K., Boilot, J.-P. & Gacoin, T. Optically anisotropic thin films by shear-oriented assembly of colloidal nanorods. *Adv. Mater.* **25,** 3295–3300 (2013).
29. Lodge, A. S. Variation of flow birefringence with stress. *Nature* **176,** 838–839 (1955).
30. Philippoff, W. Flow-birefringence and stress. *Nature* **178,** 811–812 (1956).
31. Philippoff, W. Stress-optical analysis of fluids. *Rheol. Acta* **1,** 371–375 (1961).
32. Sutera, S. P. & Wayland, H. Quantitative analysis of two-dimensional flow by means of streaming birefringence. *J. Appl. Phys.* **32,** 721–730 (1961).
33. Fuller, G. G. Optical rheometry. *Annu. Rev. Fluid Mech.* **22,** 387–417 (1990).
34. Cressely, R., Hocquart, R., Wydro, T. & Decruppe, J. P. Numerical evaluation of extinction angle and birefringence in various directions as a function of velocity gradient. *Rheol. Acta* **24,** 419–426 (1985).
35. Leal, L. G. *Advanced Transport Phenomena: Fluid Mechanics and Convective Transport Processes* (Cambridge Univ. Press, 2006).
36. Ober, T., Haward, S., Pipe, C., Soulages, J. & McKinley, G. Microfluidic extensional rheometry using a hyperbolic contraction geometry. *Rheol. Acta* **52,** 529–546 (2013).

Acknowledgements

The authors thank C. Frot and N. Taccoen for the fabrication of microfluidic channels, C. Henry de Villeneuve for atomic force microscopy and A. Agrawal for graphics. This research was partially supported by LASERLAB-EUROPE (grant agreement no. 284464 from the European Community's Seventh Framework Programme). G.A., E.F. and C.N.B. acknowledge funding by the ERC under grant agreement 278248 (Multicell).

Author contributions

J.K., J.-P.B., J.P. and T.G. developed the concept. J.K. performed synthesis, fabrication and characterizations. S.M. performed computational analysis. J.K. and M.H. performed polarized photoluminescence measurements. J.K., E.F., M.H., E.C. and G.A. performed microfluidic experiments. L.M. and M.H. prepared optical set-ups. J.K., L.M. and J.P. performed polarization analysis. C.N.B. and A.M.B. provided advice regarding the research. T.G. and J.P. supervised the research. All authors contributed to writing the manuscript.

Additional information

Supplementary information is available in the online version of the paper. Reprints and permissions information is available online at www.nature.com/reprints. Publisher's note: Springer Nature remains neutral with regard to jurisdictional claims in published maps and institutional affiliations. Correspondence and requests for materials should be addressed to J.K. and T.G.

Competing financial interests

The authors declare no competing financial interests.

Methods

Synthesis of $LaPO_4$:Eu nanorods. Aqueous solutions of $La(NO_3)_3$ (0.04 M), $Eu(NO_3)_3$ (0.01 M) and $(NH_4)_2HPO_4$ (0.05 M) were mixed at 0 °C and then vigorously stirred for 1–2 min, resulting in an instant precipitation of $LaPO_4$:Eu seed rods with a milky aspect. The mixture was transferred into a lab-made glass tube reactor and sealed to endure high pressure. The reactor was rapidly heated to 170 °C and left for 3 h without stirring. The product was centrifuged at 11,000 r.p.m. for 1 h and the pellet was re-dispersed in a 0.01 M nitric acid solution. Further purification was conducted by dialysis in a 0.01 M aqueous nitric acid solution for more than two days using a dialysis membrane (Spectra/Por, MWCO = 12,000–14,000). The aqueous $LaPO_4$:Eu nanorods obtained in this way were then transferred into ethylene glycol by distillation using a rotary evaporator. The nematic liquid-crystalline phase was obtained by controlling the final rod-volume fraction and the ionic concentration as described in the ref. 15.

Fabrication of rods oriented films. A lab-made blade coating machine was used for the directed assembly of $LaPO_4$:Eu nanorods. A 20 µl volume of nematic 'gel' phase suspension was deposited on a glass substrate. The substrate was dragged under a fixed coating blade with a constant speed (~500 µm s^{-1}) and a gap thickness of 50 µm. The coated part was continuously heated on the heating plate at 140 °C to evaporate solvent. More detail is provided in ref. 28.

Optical microscopy measurements. A conventional optical microscope (Olympus BX51WI) equipped with a charge-coupled device (CCD) camera (DTA 1600A) was used for the polarized fluorescence and birefringence measurements presented in Fig. 2. Birefringence was measured using a Berek compensator and also from the transmission images of the samples captured between crossed polarizers. Photoluminescence of $LaPO_4$:Eu was excited by a light-emitting diode illuminator (Roithner Laser Technik InGaN-SMB1W-395 nm/100 mW), producing an emission peak of 14 nm half width centred at 395 nm, which covers the $^7F_0$–$^5L_6$ transition (λ = 394 nm) of Eu^{3+} ions doped in a $LaPO_4$ crystal matrix. The photoluminescence emission from samples was filtered by a polarizer and analysed with a monochromator (SpectraPro ARC 300i) equipped with a liquid-nitrogen-cooled CCD detector. The photoluminescence tomography measurements (for the local stress-optical analysis) presented in Fig. 3 were performed using a customized laser-scanning confocal microscopy (SCM) system. The set-up had three parts: (1) an excitation laser source comprising a Ti:sapphire laser (Chameleon ULTRA-2, Coherent) combined with a second harmonic generator (APE); (2) an optical microscope (Olympus IX71, UPlanSApo objective, ×100, 1.4 NA) equipped with a piezo-scanning stage (Physik Instrument GmbH); and (3) detectors, comprising single-photon avalanche diodes (PerkinElmer) and a cooled electron-multiplying (EM) CCD camera (PhotonMax 512B, Roper Scientific) connected to the spectrometer (ARC SpectraPro 150). A monochromatic (394 nm) laser with an intensity of a few mW was guided to the sample fluidic channels through the objective. The photoluminescence signals in different polarization states and at different wavelength ranges were obtained with an analyser and bandpass filters (Semrock, FF01-578/16-25 and FF01-600/14-25) placed between the pinhole and the detectors. The resolution limit of the confocal system with 394 nm excitation was ~200 nm in x–y plane and 1 µm in the z direction (observation axis).

Electro-optical measurement. A commercial homeotropic electro-optical cell from Instec (Supplementary Fig. 1) was used to measure the polarized photoluminescence from the nematic $LaPO_4$:Eu nanorod suspension in both transverse and homeotropic orientations. A 10 µl volume of the sample suspension was injected into a 20-µm-thick cell gap through the cell opening. A function generator connected with a voltage amplifier (FLC-A400D) was used to apply a high-frequency alternating electric field (1 V μm^{-1}, 100 kHz) with zero offset to avoid the short-circuit problem.

Single-particle spectroscopy. Polarized photoluminescence from a single nanorod was measured in three steps: (1) mapping the positions and orientations of nanorods, sparsely deposited on a substrate with gold microgrills, by atomic force microscopy (AFM); (2) detecting the polarized emission spectra on the known positions by SCM; and (3) checking the precise orientation angle of each nanorod by SEM. Supplementary Fig. 3 presents corresponding SCM, AFM, and SEM pictures in different scales, used for tracking of a single nanorod.

Microfluidic experiments. A 100-µl-volume glass syringe (Hamilton) and a syringe pump (KD Scientific) were used to create a flow of the $LaPO_4$:Eu nanorod suspension. A 1-mm-diameter quartz capillary tube was used as a flow channel for the experiment corresponding to Fig. 2b. Lab-made microfluidic channels with cross-section dimensions of 100 × 50 μm^2 and 50 × 50 μm^2 with a constriction were used for the experiments corresponding, respectively, to Figs 2c–f and 3. Lab-made channels were attached on 200-µm-thick glass coverslips as bottom substrates to facilitate the local photoluminescence measurement by SCM.

Computational analysis. The flow velocity and its gradient were obtained numerically using boundary integral methods[37]. The dynamics of individual rods in response to local shear and flow rotation were obtained by generalizing the classical Jeffery's orbits of elongated particles[38]. The probability distribution of the particle's orientation was then computed numerically to obtain the distribution of f and $\dot{\gamma}_{app}$ using the stress-optical law.

Data availability. The data sets generated during and/or analysed during the current study are available from the corresponding author upon reasonable request.

References

37. Elschner, J. & Pozrikidis, C. Boundary integral and singularity methods for linearized viscous flow. *J. Appl. Math. Mech.* **74,** 104–104 (1994).
38. Jeffery, G. B. The motion of ellipsoidal particles immersed in a viscous fluid. *Proc. R. Soc. Lond. A* **102,** 161–179 (1922).

nature nanotechnology

SUPPLEMENTARY INFORMATION

DOI: 10.1038/NNANO.2017.111

In the format provided by the authors and unedited.

Supplementary Information to "Monitoring the orientation of rare-earth doped nanorods for flow shear tomography"

J. Kim, S. Michelin, M. Hilbers, L. Martinelli, E. Chaudan, G. Amselem, J.-P. Boilot, A. M. Brouwer, C. Baroud, J. Peretti, and T. Gacoin

I. EXPERIMENTAL PROCEDURES

A. Measurement of photoluminescence spectra in transverse (σ, π) and homeotropic (α) configurations

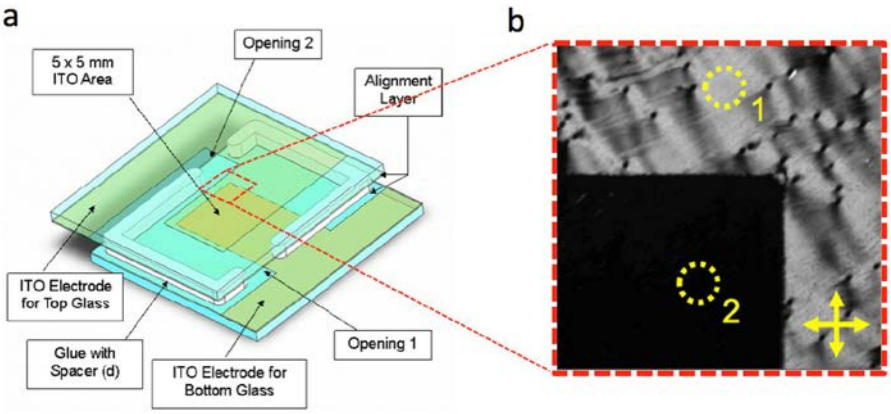

Supplementary Fig. S1. **Electro-optic measurements.** (a) Schematic of the homeotropic switching cell (Instec Inc, figure taken from the product brochure). (b) Optical transmission image (same as Figure 2d in the main script) between crossed polarizers (indicated by arrows) of the cell filled with a nematic $LaPO_4$:Eu nanorod suspension with an applied alternating electric field (1 V/m, 100 kHz). The image area is 1.8 mm × 1.8 mm.

B. Sample preparation for single nanorod photoluminescence spectroscopy

For measuring the polarized luminescence spectra of a single nanorod of known size and orientation, the particles were deposited on a patterned substrate and a procedure was developed which allows to determine by AFM and SEM the rod dimensions as well as its position and orientation with respect to the pattern (Supplementary Figure S2).

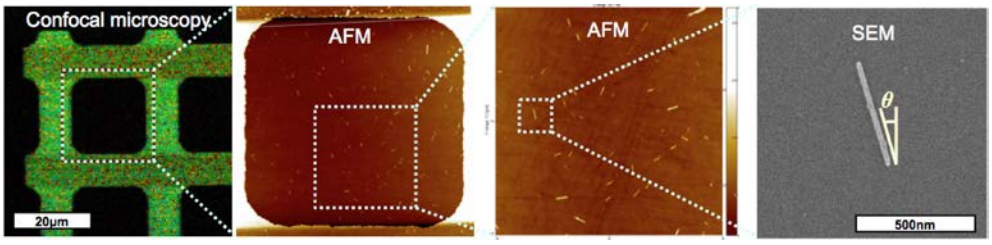

Supplementary Fig. S2. **Single nanorod sample preparation.** From left to right - Scanning confocal microscopy image of a quartz substrate with gold micro-grills on which the LaPO4:Eu nanorods were deposited; atomic force microscopy (AFM) image of a grid cell; AFM zoom image where individual nanorods are visible; SEM image of a single nanorod selected on the AFM image.

II. ANALYSIS OF THE LUMINESCENCE POLARIZATION

A. Spectral deconvolution of sublevels

The deconvolution of the sublevels' contributions was based on the analysis of the polarized PL spectra collected from the aligned nanorods' film shown in Figure 2a of the main text. Focusing on the $^5D_0$-$^7F_1$ magnetic dipolar (MD) transition (Supplementary Figure S3.b), there exist three peaks at 587.5 nm, 590.7 nm, and 595.1 nm that correspond to the three degenerate sublevels and one satellite peak at 597.4 nm.

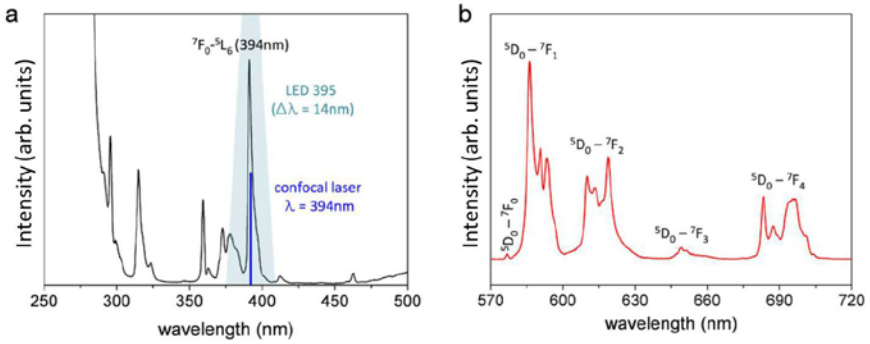

Supplementary Fig. S3. **Photoluminescence of LaPO4:Eu nanorods.**(a) Excitation spectrum of LaPO4:Eu nanorods obtained at the highest emission peak ($\lambda = 587.5$ nm). The blue region corresponds to the LED excitation source. The high absorption cross-section of the $^7F_0$-$^5L_6$ transition at the violet edge of the visible range (394 nm) allowed the use of standard optical apparatus for obtaining intense PL spectra. (b) Full emission spectrum of $LaPO_4$:Eu nanorods obtained under charge transfer band (CTB) excitation at 260 nm.

The peak deconvolution and fitting analysis were performed using the OPUS software. The best fitting peak lineshape was found to be 40%-Lorentzian and 60%-Gaussian. The spectral width of the LED excitation source (HWHM = 14 nm) broadly covering the narrow excitation peak of the $^7F_0$-$^5L_6$ transition (Supplementary Figure S3.a) seems to be responsible for the Gaussian broadening. Almost purely Lorentzian distribution was indeed found for the spectra taken with a narrow laser excitation source on the confocal microscope.

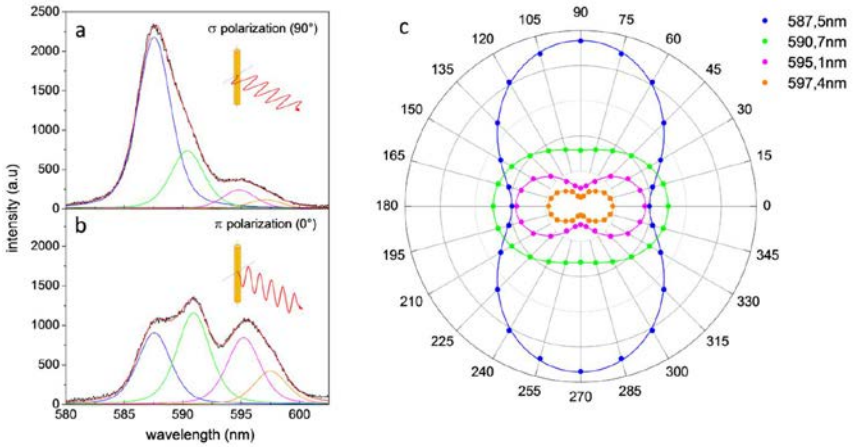

Supplementary Fig. S4. **Polarized photoluminescence of LaPO4:Eu nanorods.** σ-(a) and π-(b) polarized spectra on the $^5D_0$-$^7F_1$ MD transition with the fitted spectra (red line) as the sum of four deconvoluted peaks. (c) Polar diagram of the four peak intensities as a function of the analyzer angle varied by 15° steps corresponding to Figure 2a in the main text. The solid lines are dipolar fittings according to Eq. S1.

The fitting result for the σ and π spectra plotted in (Supplementary Figure S4.a-b clearly shows the intensity of these four peaks vary in different way indicating the low symmetry of the $LaPO_4$:Eu crystals in the hexagonal rhabdophane phase. (Supplementary Figure S4.c is a polar diagram of the peak intensities taken at each 15° steps of the rotating analyzer. The discrete data points were fitted with the orthogonal dipolar components as:

$$I = A \cdot \sin^2\theta + B \cdot \cos^2\theta \tag{S1}$$

where I is the measured peak intensity and θ is the angle between the rod orientation and the polarizer.

The very good agreement between the fit and experimental data supports the deconvolution result. Supplementary Figure S5 shows each polar diagram together with the orthogonal dipolar components plotted as red lines. As described in the main text, $^5D_0$-$^7F_1$ is a magnetic dipolar transition level where the PL emission is polarized orthogonal to the magnetic dipolar axis. The A and B values and their standard errors obtained from the fitting analysis are noted in Table I. The angle ψ between each dipole and the rod axis are also indicated. These angles reflect the dipolar geometry resulting from the crystal field splitting of sublevels. The very similar ψ values for the peaks at 595.1 nm and 597.4 nm indicate that they originate from the same sublevel.

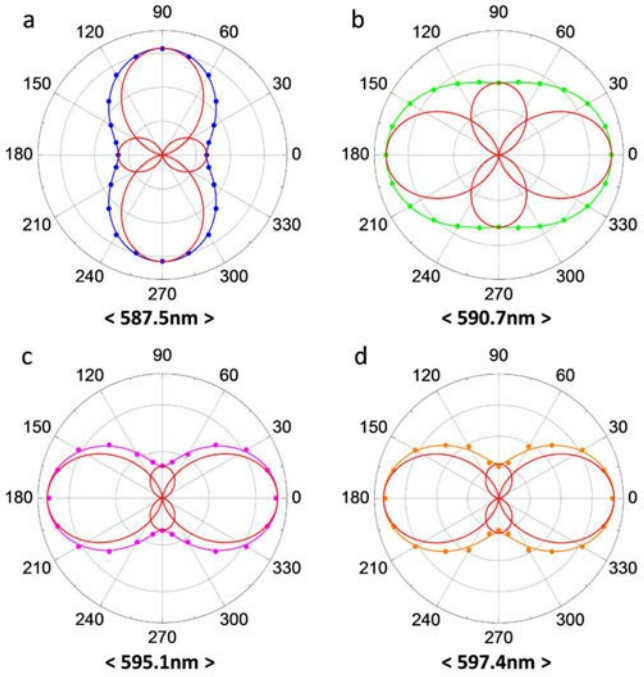

Supplementary Fig. S5. **Polar diagram of the intensity of the each peak of the $^5D_0$-$^7F_1$ MD transition.** The symbols correspond to the measurements and the full lines to the fits by two orthogonal dipolar components (red lines).

TABLE I. **dipolar components of the different contribution to the MD transition.** Intensities (in arbitrary units) and standard errors (S.E) of the orthogonal dipolar components (A, B) obtained from the fit of the polar emission diagram. The angle (ψ) between each dipole axis and the rod axis (crystallographic c-axis) is indicated.

peak	587.5 nm	590.7 nm	595.1 nm	597.4 nm
A	9422	3191	1025	553
S.E	21.8	4.4	19.3	15.4
B	3899	4979	3700	1852
S.E	20.7	4.2	18.3	14.6
ψ (deg.)	67.5	32.7	15.5	16.6

B. Determination of the nanorod orientation

1. *Single nanorod*

As demonstrated above, each sublevel transition dipole, with a particular angle ψ with respect to the rod axis, can be decomposed into two orthogonal components parallel and perpendicular to the rod axis. Regarding the uniaxial crystalline symmetry of $LaPO_4$:Eu nanorod, the perpendicular component can be considered as two orthogonal components with an identical intensity for convenience (along the x and y axis on the plane perpendicular to the rod axis). Due to the different correlations among the σ, π, and α polarization components in the electric dipolar transition (ED) and the magnetic dipolar transition (MD) described in the main text, the total emission intensity of a nanorod can be expressed as:

$$\sum I_{ED} = 2I_\pi + 2I_\sigma + 2I_\alpha = 2I_\pi + 4I_\sigma \tag{S2}$$

$$\sum I_{MD} = 2I_\pi + 2I_\sigma + 2I_\alpha = 4I_\pi + 2I_\sigma \tag{S3}$$

Considering a nanorod with an orientation (θ, φ) with respect to the laboratory frame as shown in Figure 2g of the main text, the intensities I_{xz} and I_{xy} of the polarization components along $z-$ and $y-$axis respectively, measured in the direction of observation along $x-$axis, can be expressed as a function of I_π and I_σ.

For the ED emission, one obtains:

$$I_{xz} = I_\pi \cdot \cos^2\theta + I_\sigma \cdot \sin^2\theta \tag{S4}$$

$$I_{xy} = I_\pi \cdot \sin^2\theta \cdot \sin^2\varphi + I_\sigma \cdot \left(\cos^2\theta \cdot \sin^2\varphi + \cos^2\varphi\right) \tag{S5}$$

Then, fitting the full emission spectrum $I_{xy}(\lambda)$ by a linear combination of $I_\pi(\lambda)$ and $I_\sigma(\lambda)$ obtained from the measurement of a nematic nanorod suspension in an electro-optic cell, the θ value can be directly obtained using Eq. S4. Subsequently, the φ value can be obtained from Eq. S5. It is also possible to selectively measure the emission intensities of different peaks (or bands) in the spectrum by using band path filters and a photo-detector. As each peak has a distinct polarization angle determined by the corresponding dipole orientation ψ with respect to the rod c-axis, the fitting of the whole spectrum line shape can be replaced by the analysis of two selected peaks. For each peak (refered to as $n = 1$ or 2) Eq. S5 holds and relates I_{nxy} to $I_{n\pi}$ and $I_{n\sigma}$. The value of $cos^2\theta$ can then be simply deduced from the ratio $k_{xz} = I_{1xz}/I_{2xz}$ according to the following equation :

$$cos^2\theta = \frac{k_{xz} \cdot I_{2\sigma} - I_{1\sigma}}{k_{xz} \cdot (I_{2\sigma} - I_{2\pi}) - (I_{1\sigma} - I_{1\pi})} \tag{S6}$$

Once the value of $cos^2\theta$ is obtained, the $cos^2\varphi$ value can be calculated in the same way using Eq. S5. There exist two symmetric orientations for each θ and φ correponding to the obtained values of $cos^2\theta$ and $cos^2\varphi$. Measuring one more polarized spectra at an intermediate analysis angle between x- and y-axis (at 45° for example) enables to exclude two mirror images for φ. The elimination of the mirror image of θ requires one more measurement in another direction of observation. This is technically possible by tilting the sample or using a large aperture microscope objective with a diaphragm at different positions.

For the MD transitions, equations similar to Eqs. S4-S6 can be written (see Eq.1-2 in the main text),

$$I_{xz} = I_\sigma \cdot \sin^2\theta \cdot \sin^2\varphi + I_\pi \cdot \left(\cos^2\theta \cdot \sin^2\varphi + \cos^2\varphi\right) \tag{S7}$$

$$I_{xy} = I_\sigma \cdot \cos^2\theta + I_\pi \cdot \sin^2\theta \tag{S8}$$

In this case, $cos^2\theta$ can be deduced from the ratio $k_{xy} = I_{1xy}/I_{2xy}$ of two values of I_{xy} measured at two different wavelength in the MD emission band:

$$cos^2\theta = \frac{k_{xy} \cdot I_{2\pi} - I_{1\pi}}{k_{xy} \cdot (I_{2\pi} - I_{2\sigma}) - (I_{1\pi} - I_{1\sigma})} \tag{S9}$$

Therefore, both ED and MD emission can be used to detect the orientation of a single nanorod.

2. Partially oriented nanorods suspension $(0 < f < 1)$ *along a known director* $\vec{n}$

The orientation state of a colloidal suspension containing many nanorods is defined by two quantities: the order parameter f and its director $\vec{n}$. The order parameter quantifies the local dispersion in the particle's orientation : $f = 1$ when all particles have locally the same orientation, while $f = 0$ for a fully disordered system. The observed polarized emission spectra from a local volume is an averaged sum of the emission from all the nanorods residing in the volume that have a certain orientation distribution in θ and φ with respect to $\vec{n}$. When the nanorods are submitted to an external field such as electric field or flow shear, or oriented by the spontaneous LC organization, $\vec{n}$ can often be found directly from the direction of the external field. In this case, two polarization components parallel and perpendicular to $\vec{n}$ can be noted as $I_{\parallel}$ and $I_{\perp}$ (Figure 2h in the main text) which have the same form as I_{xz} and I_{xy} for the case of a single nanorod.

For the ED emission, one has:

$$I_{\parallel} = \langle I_{\pi} \cdot \cos^2\theta + I_{\sigma} \cdot \sin^2\theta \rangle \tag{S10}$$

$$I_{\perp} = \langle I_{\pi} \cdot \sin^2\theta \cdot \sin^2\varphi + I_{\sigma} \cdot \left(\cos^2\theta \cdot \sin^2\varphi + \cos^2\varphi\right) \rangle \tag{S11}$$

where the sign $\langle\ \rangle$ stands for the average over many nanorods. Since $\vec{n}$ is a cylindrical symmetry axis, $\langle sin^2\varphi \rangle = \langle cos^2\varphi \rangle = 1/2$ and thus Eqs. S10 and S11 can be written as:

$$I_{\parallel} = I_{\pi} \cdot \langle cos^2\theta \rangle + I_{\sigma} \cdot \left(1 - \langle cos^2\theta \rangle\right) \tag{S12}$$

$$I_{\perp} = \frac{I_{\pi}}{2} \cdot \left(1 - \langle cos^2\theta \rangle\right) + \frac{I_{\sigma}}{2} \cdot \left(1 + \langle cos^2\theta \rangle\right) \tag{S13}$$

The $\langle cos^2\theta \rangle$ value can then be obtained in the same way as the value of $cos^2\theta$ for a single nanorod using $k_{\parallel} = I_{1\parallel}/I_{2\parallel}$, the ratio of two values of $I_{\parallel}$ measured at two different emission wavelength:

$$\langle cos^2\theta \rangle = \frac{k_{\parallel} \cdot I_{2\sigma} - I_{1\sigma}}{k_{\parallel} \cdot (I_{2\sigma} - I_{2\pi}) - (I_{1\sigma} - I_{1\pi})} \tag{S14}$$

For the MD emission, similar equations, shown as Eqs. 3-4 in the main text, can be written:

$$I_{\parallel} = \frac{I_{\sigma}}{2} \cdot \left(1 - \langle cos^2\theta \rangle\right) + \frac{I_{\pi}}{2} \cdot \left(1 + \langle cos^2\theta \rangle\right) \tag{S15}$$

$$I_{\perp} = I_{\sigma} \cdot \langle cos^2\theta \rangle + I_{\pi} \cdot \left(1 - \langle cos^2\theta \rangle\right) \tag{S16}$$

And again $\langle cos^2\theta \rangle$ can be deduced from the ratio $k_{\parallel}$ of two values of $I_{\parallel}$:

$$\langle cos^2\theta \rangle = \frac{k_{\parallel} \cdot (I_{2\sigma} + I_{2\pi}) - (I_{1\sigma} + I_{1\pi})}{k_{\parallel} \cdot (I_{2\sigma} - I_{2\pi}) - (I_{1\sigma} - I_{1\pi})} \tag{S17}$$

Then, from the obtained value of $\langle cos^2\theta \rangle$, one can deduce the value of $f = \left(3\langle cos^2\theta \rangle - 1\right)/2$.

3. *General solution for unknown order parameter f and unknown director $\vec{n}$*

When $\vec{n}$ is unknown, the angular orientation of $\vec{n}$ with respect to the laboratory frame (θ', φ') has first to be determined. The measured polarized PL intensities, I_{xz} and I_{xy}, can be expressed as a function of $I_{\parallel}$ and $I_{\perp}$ defined above in the form of equations similar to Eqs. S4-S5. For both ED and MD emission, one gets:

$$I_{xz} = I_{\parallel} \cdot \cos^2\theta' + I_{\perp} \cdot \sin^2\theta' \tag{S18}$$

$$I_{xy} = I_{\parallel} \cdot \sin^2\theta' \cdot \sin^2\varphi' + I_{\perp} \cdot \left(\cos^2\theta' \cdot \sin^2\varphi' + \cos^2\varphi'\right) \tag{S19}$$

For ED emission, by substituting Eqs. S12-S13 in Eq. S18, one obtains:

$$I_{xz} = \frac{I_{\pi}}{2} \cdot \left(1 - \langle\cos^2\theta\rangle - \cos^2\theta' + 3\langle\cos^2\theta\rangle \cdot \cos^2\theta'\right) + \frac{I_{\sigma}}{2} \cdot \left(1 + \langle\cos^2\theta\rangle + \cos^2\theta' - 3\langle\cos^2\theta\rangle \cdot \cos^2\theta'\right) \tag{S20}$$

Similarly to Eq. S6, the intensity ratio of two distinct peaks in one spectrum ($k_{xz} = I_{1xz}/I_{2xz}$) provides the following equation for $\langle\cos^2\theta\rangle$ and $\cos^2\theta'$:

$$\langle\cos^2\theta\rangle + \cos^2\theta' - 3\langle\cos^2\theta\rangle \cdot \cos^2\theta' = -\frac{k\,(I_{2\sigma} + I_{2\pi}) - (I_{1\sigma} + I_{1\pi})}{k\,(I_{2\sigma} - I_{2\pi}) - (I_{1\sigma} - I_{1\pi})} \tag{S21}$$

For MD emission, by substituting in Eq. S18 the expressions $I_{\parallel}$ and $I_{\perp}$ given by Eqs. S15-S16, one obtains:

$$I_{xz} = \frac{I_{\sigma}}{2} \cdot \left(2\langle\cos^2\theta\rangle + \cos^2\theta' - 3\langle\cos^2\theta\rangle \cdot \cos^2\theta'\right) + \frac{I_{\pi}}{2} \cdot \left(2 - 2\langle\cos^2\theta\rangle - \cos^2\theta' + 3\langle\cos^2\theta\rangle \cdot \cos^2\theta'\right) \tag{S22}$$

$$2\langle\cos^2\theta\rangle + \cos^2\theta' - 3\langle\cos^2\theta\rangle \cdot \cos^2\theta' = -2 \cdot \frac{k_{xz} \cdot I_{2\pi} - I_{1\pi}}{k_{xz} \cdot (I_{2\sigma} - I_{2\pi}) - (I_{1\sigma} - I_{1\pi})} \tag{S23}$$

Therefore, the two unknown values of $\langle\cos^2\theta\rangle$ and $\cos^2\theta'$ can be determined from Eqs. S21 and S23 from ED and MD. The value of $\cos^2\varphi'$ can then be calculated using Eq. S19. Finally, the mirror values of φ' can be eliminated in the same way as indicated for the case of a single nanorod.

4. *Calculation of f and $\vec{n}$ on the microfluidic channel cross-sections*

The determination of f and $\vec{n}$ from experiments performed in a microfluidic channel with a constriction as described in the main text was achieved using the above equations that were simplified taking into account the boundary conditions. Polarized PL measurements on a single transition level (preferably a MD transition that exhibits more dramatic line shape change than an ED transition) provides sufficient information. In the case of the vertical section (Figure 4a, 4c-left, and 4d in the main text), as $\vec{n}$ is constantly normal to the scanning plane, Eqs. S15-S16 were used to obtain $\langle\cos^2\theta\rangle$ and f. In the case of the horizontal section across the constriction (Figure 4a, 4c-right, and 4e in the main text) located at the middle height of the channel, the value of φ' is fixed at 90° and thus Eq. S19 simplifies as:

$$I_{xy} = I_{\parallel} \cdot \sin^2\theta' + I_{\perp} \cdot \cos^2\theta' \tag{S24}$$

To eliminate the mirror images of φ', an additional equation for the measurement at the analyzer angle of 45° can be expressed as:

$$I_{x45^\circ} = I_{\parallel} \cdot \cos^2\left(\frac{\pi}{4} - \theta'\right) + I_{\perp} \cdot \sin^2\left(\frac{\pi}{4} - \theta'\right)$$
$$= \frac{I_{\parallel}}{2} \cdot (1 + sin2\theta') + \frac{I_{\perp}}{2} \cdot (1 - sin2\theta')$$
$$= \frac{I_{\parallel} + I_{\perp}}{2} + sin2\theta' \cdot \frac{I_{\parallel} - I_{\perp}}{2} \quad \text{(S25)}$$

From Eq. S18 and S25 one can obtain:

$$tan2\theta' = \frac{2I_{x45^\circ} - I_{xz} - I_{xy}}{I_{xz} - I_{xy}} \quad \text{(S26)}$$

Considering θ' ranges between 90° and −90°, the solution for θ' can be expressed as:

$$\theta' = \frac{1}{2}\left[arctan\left(\Sigma\right) - \frac{\pi}{2} \cdot \frac{\Sigma}{|\Sigma|}\left(\frac{\Gamma}{|\Gamma|} + 1\right)\right] \quad \text{(S27)}$$

where,

$$\Sigma = \frac{2I_{x45^\circ} - I_{xz} - I_{xy}}{I_{xz} - I_{xy}} \quad \text{and} \quad \Gamma = I_{xz} - I_{xy}$$

The values of $I_{\parallel}$ and $I_{\perp}$ were obtained with the value of θ' using Eq. S18 and S24. The values of $\langle\cos^2\theta\rangle$ and f were then obtained using Eq. S15-S16.

C. Determination of the apparent shear rate $\dot{\gamma}_{app}$

The apparent shear rate at each focal point in the microfluidic channel can be deduced from the value of f using the stress optical law shown in Supplementary Figure S6a. This curve is obtained by fitting the experimental (polarized luminescence and birefringence) data obtained on a linear microfluidic channel with the model described in the next section (see Figure 3f in the main text).

The uncertainty $\Delta\dot{\gamma}_{app}$ on the determination of $\dot{\gamma}_{app}$ is related to the uncertainty Δf on the experimental determination of f by the slope of the stress optical law:

$$\Delta\left(\dot{\gamma}_{app}/\Omega\right) = \frac{\partial\left(\dot{\gamma}_{app}/\Omega\right)}{\partial f}\Delta f. \quad \text{(S28)}$$

The sensitivity of the measurement to the value of the apparent shear rate is then characterized by the ratio:

$$\frac{\dot{\gamma}_{app}}{\Delta\dot{\gamma}_{app}} = \frac{F}{\Delta f} \quad \text{(S29)}$$

where

$$F = \left(\dot{\gamma}_{app}/\Omega\right) \cdot \frac{\partial f}{\partial\left(\dot{\gamma}_{app}/\Omega\right)} \quad \text{(S30)}$$

defines the figure of merit for the determination of the apparent shear rate (Supplementary Figure S6b).

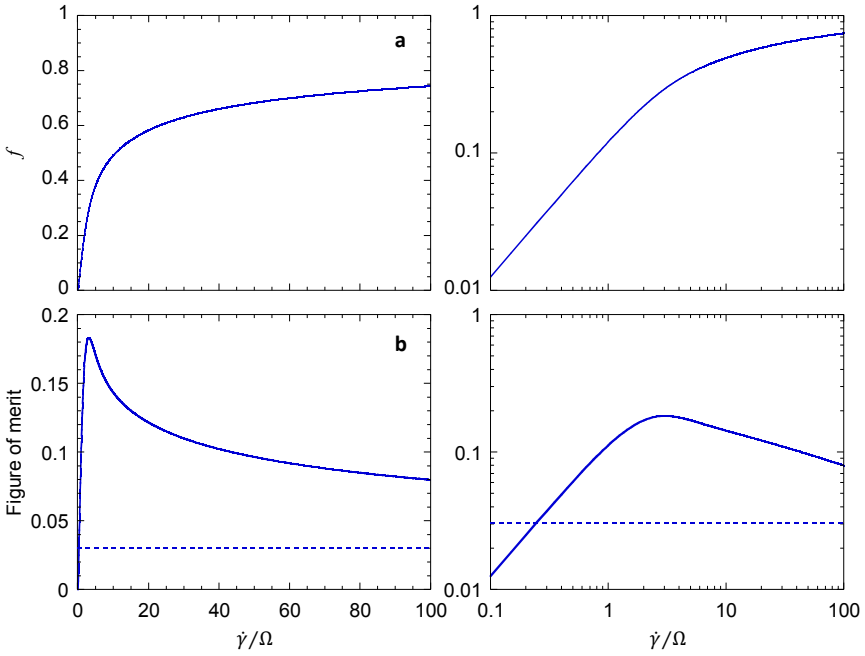

Supplementary Fig. S6. **Relation between the apparent shear rate and the order parameter.**(a) Order parameter f as a function of the shear-rate-to-diffusion ratio for a plane parallel shear flow. (b) Figure of merit F for the experimental determination of the apparent shear rate. log-log plots of the same quantities are also shown (right).

From the expressions of $\langle \cos^2 \theta \rangle$ given in the previous sections, it can easily be shown that:

$$\Delta f \approx \frac{\Delta I}{I} \tag{S31}$$

where I is the number of photons detected at a single focal point of the 3D photoluminescence mapping of the channel in a narrow band around the chosen transition wavelength (for instance, $I = I_{1xz}$). In the experiment reported here, the typical value of I is of the order of a few 1000 for the highest resolution (the probed confocal volume is $\sim 1\ \mu m^3$) and measurements are shot-noise limited. Therefore, $\Delta f \approx 1/\sqrt{I} \approx 1/30$ (dashed line in Supplementary Figure S6b) and the ratio $\dot{\gamma}_{\rm app}/\Delta\dot{\gamma}_{\rm app}$ is larger than unity over a range. When downgrading the resolution by about a factor of 2, the probed volume and the number of detected photons increase by about an order of magnitude and the uncertainty on the determination of the shear rate becomes less than 10% for $\dot{\gamma}_{\rm app}/\Omega$ ranging from 0.1 to several 100 (while, in the present case, the fitting of the stress-optical law gives $\Omega = 0.5\ s^{-1}$).

III. MODELING THE SHEAR FLOW AND THE PARTICLE ORIENTATION

A. Particle reorientation in viscous flows

A simplified two-dimensional model is proposed here for the particle reorientation dynamics in the geometry of Figure 4 of the main text, based on two main assumptions: (i) the flow is purely two-dimensional and (ii) each particle (i.e. slender rods of length a and diameter b with $\rho = a/b \gg 1$) lies in the (x, y) shear plane, its orientation being defined by its polar angle φ (see Supplementary Figure S7).

For a small rod-like particle (i.e. $b \ll a \ll H$), the evolution of φ is described as (Jeffery's orbits, [2])

$$\dot{\varphi} = \frac{\omega + \dot{\gamma}\cos(2\varphi - 2\Phi)}{2}, \tag{S32}$$

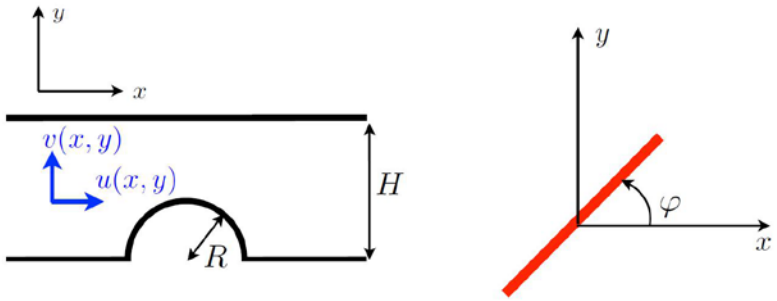

Supplementary Fig. S7. **Definition of the particle's orientation.**

where $\omega(x,y)$, $\Phi(x,y)$ and $\dot{\gamma}(x,y)$ are the local vorticity, principal shear direction and modulus, respectively:

$$\omega = \frac{\partial v}{\partial x} - \frac{\partial u}{\partial y}, \quad \dot{\gamma} = \sqrt{\left(\frac{\partial u}{\partial x} - \frac{\partial v}{\partial y}\right)^2 + \left(\frac{\partial u}{\partial y} + \frac{\partial v}{\partial x}\right)^2}. \tag{S33}$$

B. Reorientation dynamics in a dilute suspension

For dilute suspensions of such particles in steady flows, the probability density function $\psi(x,y,\varphi)$ to find a particle at location (x,y) with orientation φ satisfies [4]

$$\mathbf{u}\cdot\nabla\psi + \frac{\partial}{\partial\varphi}(\psi\dot{\varphi}) = \Omega\,\frac{\partial^2\psi}{\partial\varphi^2}, \tag{S34}$$

where the different terms describe the advection of the particles by the flow, their reorientation by the flow gradient, and their rotational diffusion. Ω is the particles' rotational diffusivity (see Eq. (5) of main text); translational diffusion is negligible here since $a \ll H$.

The order parameter, f, is obtained from ψ as:

$$f(x,y) = \sqrt{<\sin(2\varphi)>_\varphi^2 + <\cos(2\varphi)>_\varphi^2}. \tag{S35}$$

In a straight channel, $\mathbf{u}\cdot\nabla\psi = 0$, and the reorientation of particles in shear balances rotational diffusion:

$$\frac{\partial}{\partial\varphi}\left[\psi\left(\frac{\omega + \dot{\gamma}\cos(2\varphi - 2\bar{\varphi})}{2}\right)\right] = \Omega\,\frac{\partial^2\psi}{\partial\varphi^2}. \tag{S36}$$

The order parameter f then depends solely on the *local* flow vorticity ω and shear $\dot{\gamma}$. Further, for such parallel flows, $\omega = -\dot{\gamma}$, and the order parameter is a function of $\dot{\gamma}$ only: $f = g(\dot{\gamma}/\Omega)$. The resulting stress-optical law ([1], Supplementary Figure S6) can be inverted to obtain an estimation of the apparent shear rate $\dot{\gamma}_{\mathrm{app}}$:

$$\dot{\gamma}_{\mathrm{app}} = \Omega\; g^{-1}(f). \tag{S37}$$

In more complex geometries, particles' advection leads to a change in the flow experienced by each particle on a typical time scale H/U, to be compared to the rotational diffusion time scale Ω^{-1}. Their ratio is the Péclet number $\mathrm{Pe} = U/\Omega H$ and is a measure of the relative effect of advection and diffusion.

For fast diffusion ($\mathrm{Pe} \ll 1$), the particles' orientation adjusts instantaneously; Eqs. (S36) and (S37) remain valid.

For slow diffusion, ($\mathrm{Pe} = O(1)$), the full dynamics must be considered and Eq. (S34) must be solved. f now depends on the history of the flow experienced by the particles, and not only on the local flow conditions. Finding f and $\dot{\gamma}_{\mathrm{app}}$ now proceeds in two steps:

- first, find the flow velocity $\mathbf{u}$ everywhere in a given channel, its gradient, as well as the flow streamlines;
- second, solve Eq. (S34) as an evolution equation for ψ along each streamline, to obtain ψ and f everywhere.

C. Flow computations

The flow field is computed using a Boundary Integral Method [3], in a fluid domain V_f corresponding to the section $-L \leq x \leq L$ of the channel of Supplementary Figure S7 ($x = 0$ corresponds to the center of the obstacle, and $L \gg H$). The flow velocity $\mathbf{u}$ satisfies the integral equation:

$$\alpha \mathbf{u}(\mathbf{x}) = \int_{\partial V_f} \left[\mathbf{S}(\mathbf{r}) \cdot \mathbf{f}(\mathbf{x}') - \mathbf{u}(\mathbf{x}') \cdot \mathbf{T}(\mathbf{r}) \cdot \mathbf{n}(\mathbf{x}')\right] \mathrm{d}l(\mathbf{x}') \tag{S38}$$

with $\mathbf{r} = \mathbf{x} - \mathbf{x}'$, and $\alpha = 1$ (resp. $\alpha = 1/2$) for a point inside (resp. on the boundary of) the domain. $\mathbf{S}$ and $\mathbf{T}$ are the single- and double-layer potentials, respectively:

$$\mathbf{S}(\mathbf{r}) = \frac{1}{2\pi}\left(\mathbf{I}\log(r) - \frac{\mathbf{rr}}{r^2}\right), \quad \mathbf{T}(\mathbf{r}) = \frac{4\,\mathbf{rrr}}{r^4}. \tag{S39}$$

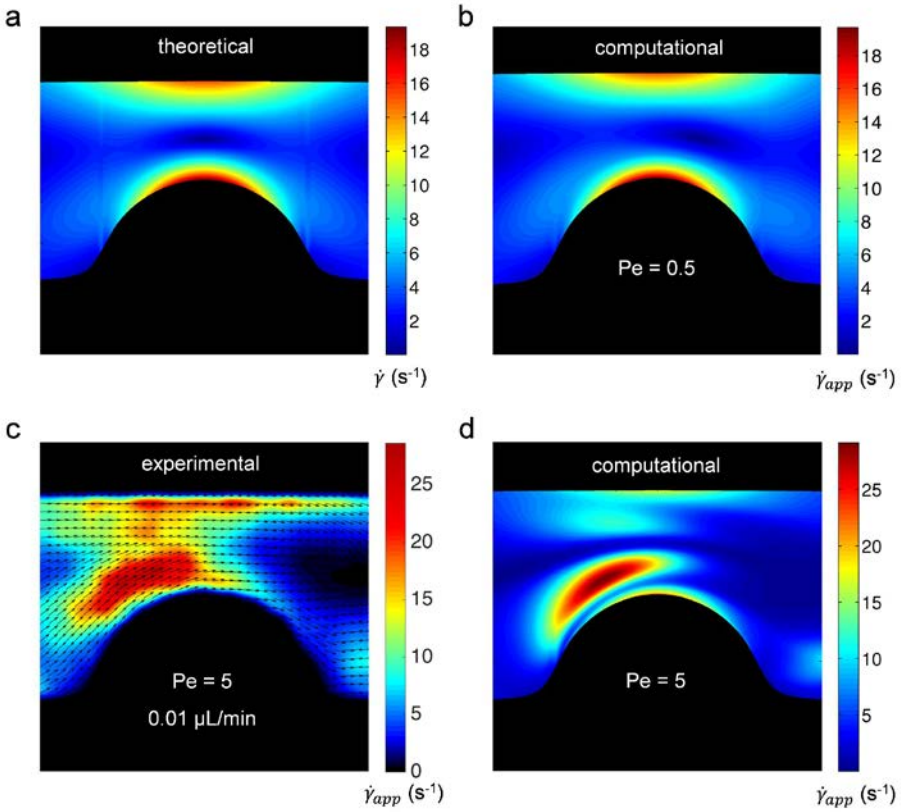

Supplementary Fig. S8. **Apparent and Actual shear rates.** Apparent shear (in s^{-1}) from the distribution of order parameter (a) measured for $\mathrm{Pe} = 5$, (b) calculated for $\mathrm{Pe} = 5$ and (d) for $\mathrm{Pe} = 0.5$. (c) Actual shear rate $\dot{\gamma}$ (s^{-1}) around the obstacle calculated for the experimental conditions $H = 50\mu$m and $U = 140\mu\mathrm{m.s}^{-1}$.

Applying Eq. (S38) on ∂V_f provides an integral equation for the boundary flow velocity and traction forces $\mathbf{f}$, which is inverted numerically by imposing no-slip ($\mathbf{u} = 0$) on the solid walls, a horizontal inlet/outlet flow velocity and a fixed pressure drop Δp between $x = \pm L$.

The flow velocity and its gradient are computed anywhere in V_f using Eq. (S38) and $\dot{\gamma}$ is found from Eq. (S33). The shear rate intensity is symmetric about the obstacle (Supplementary Figure S8a). The position of a given streamline $\mathbf{x}_s(s)$ is found by solving $\mathbf{u}(\mathbf{x}_s) \times \partial \mathbf{x}_s / \partial s = 0$.

D. Determination of the particle orientation in the channel

Equation (S34) is then solved along each streamline numerically using an implicit second order finite difference scheme. The initial condition at $x = -L$ is obtained from the classical straight channel results. From ψ, the distribution of order parameter in the entire channel and the apparent shear rate are computed using Eqs. (S35) and (S37) for different Pe (Supplementary Figure S8b and d).

For low Pe (small particles), $\dot{\gamma}_{\text{app}}$ (Supplementary Figure S8b) closely matches the actual shear rate (Supplementary Figure S8a) confirming that the quasi-steady analysis is valid. For slower diffusion (larger particles), $\dot{\gamma}_{\text{app}}$ (Supplementary Figure S8d) and $\dot{\gamma}$ (Supplementary Figure S8a) do not match anymore (in particular, $\dot{\gamma}_{\text{app}}$ is not symmetric around the obstacle as opposed to $\dot{\gamma}$). Nevertheless the simulated $\dot{\gamma}_{\text{app}}$ (Supplementary Figure S8d) matches very well the experimental observations (Supplementary Figure S8c).

[1] J. T. Edsall H. A. Scheraga and J. O. Gadd. Double refraction of flow: numerical evaluation of extinction angle and bi-refringence as a function of velocity gradient. *J. Chem. Phys.*, 19:1101, 1951.
[2] G. B. Jeffery. The motion of ellipsoidal particles immersed in a viscous fluid. *Proc. Roy. Soc. A*, 102:161–179, 1922.
[3] C. Pozrikidis. *Boundary integral and singularity methods for linearized viscous flows.* Cambridge Univ. Press, Cambridge, 1992.
[4] D. Saintillan and M. J. Shelley. Instabilities, pattern formation and mixing in active particle suspensions. *Phys. Fluids*, 20:123304, 2008.